

Redshift-space distortions of galaxies, clusters and AGN: testing how the accuracy of growth rate measurements depends on scales and sample selections

Federico Marulli^{1,2,3*}, Alfonso Veropalumbo¹, Lauro Moscardini^{1,2,3}, Andrea Cimatti¹ and Klaus Dolag^{4,5}

¹ Dipartimento di Fisica e Astronomia, Alma Mater Studiorum Università di Bologna, viale Berti Pichat 6/2, I-40127 Bologna, Italy

² INAF, Osservatorio Astronomico di Bologna, via Ranzani 1, I-40127 Bologna, Italy

³ INFN, Sezione di Bologna, viale Berti Pichat 6/2, I-40127 Bologna, Italy

⁴ Department of Physics, Ludwig-Maximilians-Universität, Scheinerstr. 1, D-81679 München, Germany

⁵ Max-Planck-Institut für Astrophysik, Karl-Schwarzschild Strasse 1, D-85748 Garching bei München, Germany

22 September 2018

ABSTRACT

Redshift-space clustering anisotropies caused by cosmic peculiar velocities provide a powerful probe to test the gravity theory on large scales. However, to extract unbiased physical constraints, the clustering pattern has to be modelled accurately, taking into account the effects of non-linear dynamics at small scales, and properly describing the link between the selected cosmic tracers and the underlying dark matter field. We use a large hydrodynamic simulation to investigate how the systematic error on the linear growth rate, f , caused by model uncertainties, depends on sample selections and comoving scales. Specifically, we measure the redshift-space two-point correlation function of mock samples of galaxies, galaxy clusters and Active Galactic Nuclei, extracted from the *Magneticum* simulation, in the redshift range $0.2 \leq z \leq 2$, and adopting different sample selections. We estimate $f\sigma_8$ by modelling both the monopole and the full two-dimensional anisotropic clustering, using the *dispersion model*. We find that the systematic error on $f\sigma_8$ depends significantly on the range of scales considered for the fit. If the latter is kept fixed, the error depends on both redshift and sample selection, due to the scale-dependent impact of non-linearities, if not properly modelled. On the other hand, we show that it is possible to get unbiased constraints on $f\sigma_8$ provided that the analysis is restricted to a proper range of scales, that depends non trivially on the properties of the sample. This can have a strong impact on multiple tracers analyses, and when combining catalogues selected at different redshifts.

Key words: cosmology: theory – cosmology: observations, dark matter, dark energy, galaxy clustering

1 INTRODUCTION

The dynamics of the Universe is shaped by the gravity force. The understanding of gravity is thus the key to unveil the nature of the Universe and its cosmological evolution. After almost one century from its original formulation, Einstein’s General Relativity (GR) is still the dominant theory to describe gravity. However, despite its lasting experimental successes, some fundamental open issues are motivating challenging efforts aimed at searching for possible expansions or radically alternative models (Amendola et al. 2013). First of all, GR is not a quantum field theory and cannot be rec-

onciled with the principles of quantum mechanics. Secondly, an increasingly large amount of astronomical observations cannot be explained by GR and baryonic matter alone, requiring the introduction of a never observed form of dark matter (DM, Zwicky 1937). Finally, independent cosmological observations give indisputable evidences for an accelerated expansion of the Universe, requiring the introduction of another dark component, generally dubbed dark energy, when interpreted in the GR framework (Riess et al. 1998; Perlmutter et al. 1999). Whether GR provides a reliable description of the large scale structure of the Universe, and thus the latter is dominated by unknown dark components, or, on the contrary, such a gravity theory has to be corrected, or even abandoned, is one of the key questions of modern physics and cosmology.

* E-mail: federico.marulli3@unibo.it

One of the most effective ways to test the gravity theory on large scales, that is where the DM and dark energy arise, is to exploit the apparent anisotropies observed in galaxy maps, the so-called redshift-space distortions (RSD, Sargent & Turner 1977; Kaiser 1987). Indeed, by modelling redshift-space clustering anisotropies it is possible to constrain the linear growth rate of cosmic structures, $f \equiv d \log \delta / d \log a$, where a is the dimensionless scale factor and δ the linear fractional density perturbation, provided that the galaxy bias is known. This method has already been successfully applied to many galaxy redshift surveys, both in the local Universe and at larger redshifts, up to $z \sim 1$, such as SDSS (Samushia, Percival & Raccanelli 2012; Chuang & Wang 2013; Chuang et al. 2013), WiggleZ (Blake et al. 2012; Contreras et al. 2013), 6dFGS (Beutler et al. 2012), BOSS (Tojeiro et al. 2012; Reid et al. 2012), VVDS (Guzzo et al. 2008), and VIPERS (de la Torre et al. 2013).

All the above measurements have been obtained from large galaxy redshift surveys. First tentative studies are starting to consider also different tracers, but results are still strongly affected by statistical uncertainties, due to the paucity of the catalogues used. Thanks to the wealth of observational data now available, or expected in the next future, for instance from the ESA Euclid mission¹ (Laureijs et al. 2011), the NASA Wide Field Infrared Space Telescope (WFIRST) mission² (Spergel et al. 2013), and the extended Roentgen Survey with an Imaging Telescope Array (eROSITA) satellite mission³ (Merloni et al. 2012) it will soon become possible to apply these methodologies on both cluster and Active Galactic Nuclei (AGN) catalogues. Galaxy clusters are the biggest collapsed structures in the Universe. They appear more strongly biased than galaxies, that is their clustering signal is higher. Moreover, they are relatively unaffected by non-linear dynamics on small scales. This could help in modelling redshift-space distortions in their clustering pattern, as the effect of small scale incoherent motions, that generate the so-called fingers-of-God pattern, is substantially less severe relative to the galaxy clustering case, improving also the cosmological constraints that can be extracted from baryon acoustic oscillations (Veropalumbo et al. 2014, in preparation). The main drawback is the low density of galaxy cluster samples and the fact that these sources can be reliably detected only at relatively small redshifts. On the other hand, AGN can be detected up to very large distances. Powered by accreting supermassive black holes hosted at their centres, their extreme luminosities make them optimal tracers to investigate the largest scales of the Universe, and thus its cosmological evolution (see e.g. Marulli et al. 2008, 2009; Bonoli et al. 2009, and references therein).

The aim of this paper is to investigate the *accuracy* of the so-called *dispersion model* (that will be described in §3) as a function of comoving scales and sample selection. To achieve this goal, we exploit realistic mock samples of galaxies, galaxy clusters and AGN extracted from the *Magneticum* hydrodynamic simulation, at six snapshots in the range $0.2 \leq z \leq 2$. We adopt a similar methodology as in Bianchi et al. (2012), though substantially extending that analysis. Specifically, i) in line with the majority of recent studies, we investigate the systematic errors of $f\sigma_8$, instead of β , ii) we consider different kinds of realistic mock tracers, instead of just DM haloes, iii) we analyse the dependency of the errors as a

function of redshift, and iv) as a function of different sample selections. In agreement with previous investigations, we find that the rough modelization of non-linear dynamics provided by the dispersion model introduces systematic errors on $f\sigma_8$ measurements, that depend non trivially on the redshift and bias of the tracers. On the other hand, as we will demonstrate, it is possible to get unbiased constraints on $f\sigma_8$ provided that the fit is restricted in a proper range of scales, that depends on sample selection.

The software that we implemented to perform all the analyses presented in this paper can be freely downloaded at this link: <http://apps.difa.unibo.it/files/people/federico.marulli3/>. It consists of a set of C++ libraries that can be used for several astronomical calculations, in particular to measure the two-point correlation function and to model RSD. We also provide the full documentation for these libraries, and some example codes that explain how to use them.

The paper is organised as follows. In §2 we describe the *Magneticum* simulation used to construct mock samples of galaxies, clusters and AGN, whose main properties are reported in Appendix A. In §3 and §4 we present the formalism used to model RSD and to measure the two-point correlation function in redshift-space mock catalogues, respectively. The results of our analyses are presented in §5. Finally, in §6 we summarise our conclusions.

2 THE MAGNETICUM SIMULATION

The most direct way to investigate systematic errors on linear growth rate measurements from RSD is to exploit large numerical simulations, and to apply on them the same methodologies used for real data. As our goal is to study the effects of different sample selections, we make use of realistic mock catalogues of different cosmic tracers. Specifically, we analyse galaxy, cluster and AGN mock catalogues extracted from the hydrodynamic *Magneticum* simulation⁴ (Dolag et al. in preparation).

This simulation is based on the parallel cosmological TreePM-SPH code P-GADGET3 (Springel 2005). The code uses an entropy-conserving formulation of smoothed-particle hydrodynamics (SPH) (Springel & Hernquist 2002) and follows the gas using a low-viscosity SPH scheme to properly track turbulence (Dolag et al. 2005). It also allows a treatment of radiative cooling, heating from a uniform time-dependent ultraviolet background and star formation with the associated feedback processes. The latter is based on a sub-resolution model for the multiphase structure of the interstellar medium (ISM) (Springel & Hernquist 2003a).

Radiative cooling rates are computed by following the same procedure presented by Wiersma, Schaye & Smith (2009). We account for the presence of the cosmic microwave background and of ultraviolet/X-ray background radiation from quasars and galaxies, as computed by Haardt & Madau (2001). The contributions to cooling from each one of the following 11 elements, H, He, C, N, O, Ne, Mg, Si, S, Ca, Fe, have been pre-computed using the publicly available CLOUDY photoionization code (Ferland et al. 1998) for an optically thin gas in photoionization equilibrium.

In the multiphase model for star-formation (Springel & Hernquist 2003b), the ISM is treated as a two-phase medium where clouds of cold gas form from cooling of hot gas and are embedded in the hot gas phase assuming pressure equilibrium whenever gas particles are above a given

¹ <http://www.euclid-ec.org>

² <http://wfirst.gsfc.nasa.gov>

³ <http://www.mpe.mpg.de/eROSITA>

⁴ www.magneticum.org

threshold density. The hot gas within the multiphase model is heated by supernovae and can evaporate the cold clouds. A certain fraction of massive stars (10 per cent) is assumed to explode as supernovae type II (SNII). The released energy by SNII (10^{51} erg) is modelled to trigger galactic winds with a mass loading rate being proportional to the star formation rate to obtain a resulting wind velocity of $v_{\text{wind}} = 350$ km/s. Our simulation also includes a detailed model of chemical evolution according to Tornatore et al. (2007). Metals are produced by SNII, by supernovae type Ia (SNIa) and by intermediate and low-mass stars in the asymptotic giant branch (AGB). Metals and energy are released by stars of different mass by properly accounting for mass-dependent lifetimes, with a lifetime function according to Padovani & Matteucci (1993), the metallicity-dependent stellar yields by Woosley & Weaver (1995) for SNII, the yields by van den Hoek & Groenewegen (1997) for AGB stars and the yields by Thielemann et al. (2003) for SNIa. Stars of different mass are initially distributed according to a Chabrier initial mass function (Chabrier 2003).

Most importantly, the *Magneticum* simulation also includes a prescription for black hole growth and for feedback from AGN. As for star formation, the accretion onto black holes and the associated feedback adopts a sub-resolution model. Black holes are represented by collisionless “sink particles” that can grow in mass by accreting gas from their environments, or by merging with other black holes. Our implementation is based on the model presented in Springel et al. (2005) and Di Matteo, Springel & Hernquist (2005), including the same modifications as in the study of Fabjan et al. (2010) and some new, minor changes, as described in Hirschmann et al. (2014).

The black hole (BH) gas accretion rate, \dot{M}_{BH} , is estimated by using the Bondi-Hoyle-Lyttleton approximation (Hoyle & Lyttleton 1939; Bondi & Hoyle 1944; Bondi 1952):

$$\dot{M}_{\text{BH}} = \frac{4\pi G^2 M_{\text{BH}}^2 f_{\text{boost}} \rho}{(c_s^2 + v^2)^{3/2}}, \quad (1)$$

where ρ and c_s are the density and the sound speed of the surrounding (ISM) gas, respectively, f_{boost} is a boost factor for the density which is typically set to 100 and v is the velocity of the black hole relative to the surrounding gas. The black hole accretion is always limited to the Eddington rate. The radiated bolometric luminosity, L_{bol} , is related to the black hole accretion rate by

$$L_{\text{bol}} = \epsilon_r \dot{M}_{\text{BH}} c^2, \quad (2)$$

where ϵ_r is the radiative efficiency, for which we adopt a fixed value of 0.1, standardly assumed for a radiatively efficient accretion disk onto a non-rapidly spinning black hole according to Shakura & Sunyaev (1973) (see also Springel 2005; Di Matteo, Springel & Hernquist 2005).

The simulation covers a cosmological volume with periodic boundary conditions initially occupied by an equal number of 1526^3 gas and DM particles, with relative masses that reflect the global baryon fraction, Ω_b/Ω_M . The box side is $896 h^{-1}$ Mpc. The cosmological model adopted is a spatially flat Λ CDM universe with matter density $\Omega_M = 0.272$, baryon density $\Omega_b = 0.0456$, power spectrum normalization $\sigma_8 = 0.809$, and Hubble constant $H_0 = 70.4 \text{ km s}^{-1} \text{ Mpc}^{-1}$, chosen to match the seven-year Wilkinson Microwave Anisotropy Probe (WMPA7, Komatsu et al. 2011). More details on the *Magneticum* simulation and the derived mock catalogues can be found in Hirschmann et al. (2014); Saro et al. (2014); Bocquet et al. (2015).

Firstly, we will analyse large samples of mock galaxies, clusters and AGN selected in stellar mass, cluster mass and BH mass,

respectively. Then, we will consider several subsamples with different selections, as reported in Tables A1, A2 and A3 (see §5).

3 REDSHIFT-SPACE DISTORTIONS

To construct redshift-space mock catalogues, we adopt the same methodology used in Bianchi et al. (2012), Marulli et al. (2011, 2012), and Marulli, Baldi & Moscardini (2012). We provide here a brief description. We consider a local virtual observer at $z = 0$, and place the centre of each snapshot of the *Magneticum* simulation at a comoving distance, D_c , corresponding to its redshift, that is:

$$D_c(z) = c \int_0^z \frac{dz'_c}{H(z'_c)}, \quad (3)$$

where c is the speed of light, and the Hubble expansion rate is:

$$H(z) = H_0 \left[\Omega_M (1+z)^3 + \Omega_k (1+z)^2 + \Omega_{\text{DE}} \exp \left(3 \int_0^z \frac{1+w(z)}{1+z} \right) \right]^{0.5}, \quad (4)$$

where $\Omega_k = 1 - \Omega_M - \Omega_{\text{DE}}$, $w(z)$ is the dark energy equation of state, and the contribution of radiation is assumed negligible. In our case: $\Omega_k = 1$, $w(z) = 1$, so $\Omega_{\text{DE}} \equiv \Omega_\Lambda = 1 - \Omega_M$ and the Hubble expansion rate reduces to:

$$H(z) = H_0 \left[\Omega_M (1+z)^3 + \Omega_\Lambda \right]. \quad (5)$$

To estimate the distribution of mock sources in redshift-space, we then transform the comoving coordinates of each object into angular positions and observed redshifts. The latter are computed as follows:

$$z_{\text{obs}} = z_c + \frac{v_{\parallel}}{c} (1+z_c), \quad (6)$$

where z_c is the *cosmological* redshift due to the Hubble recession velocity at the comoving distance of the object and v_{\parallel} is the line-of-sight component of its centre of mass velocity. In this analysis we do not include any error in the observed redshift, and neither geometric distortions caused by an incorrect assumption of the background cosmology (see Marulli et al. 2012, for more details).

In the linear regime, the velocity field can be determined from the density field, and the amplitude of RSD is proportional to the parameter β , defined as follows:

$$\beta(z) \equiv \frac{f(z)}{b(z)}, \quad (7)$$

where the linear growth rate, f , can be approximated in most cosmological frameworks as:

$$f(z) \simeq \Omega_M^\gamma(z), \quad (8)$$

with $\gamma \simeq 0.545$ in Λ CDM. The linear bias factor can be estimated as:

$$b(z) = \left\langle \sqrt{\frac{\xi(r; z)}{\xi_{\text{DM}}(r; z)}} \right\rangle, \quad (9)$$

where the mean is computed at sufficiently large scales at which non-linear effects can be neglected.

In the linear regime, the redshift-space two-point correlation function can be written as follows:

$$\xi^{\text{lin}}(s, \mu) = \xi_0(s) P_0(\mu) + \xi_2(s) P_2(\mu) + \xi_4(s) P_4(\mu), \quad (10)$$

where $\mu \equiv \cos \theta = s_{\parallel}/s$ is the cosine of the angle between the separation vector and the line of sight, $s = \sqrt{s_{\perp}^2 + s_{\parallel}^2}$, and P_l are the Legendre polynomials (Kaiser 1987; Lilje & Efstathiou 1989; McGill 1990; Hamilton 1992; Fisher, Scharf & Lahav 1994). Eq. (10) is derived in the distant-observer approximation, that is reasonable at the small scales considered in this analysis. The multipoles of $\xi(s_{\perp}, s_{\parallel})$ are:

$$\xi_0(s) = \left(1 + \frac{2}{3}\beta + \frac{1}{5}\beta^2\right) \cdot \xi(r) \quad (11a)$$

$$= \left[(b\sigma_8)^2 + \frac{2}{3}f\sigma_8 \cdot b\sigma_8 + \frac{1}{5}(f\sigma_8)^2 \right] \cdot \frac{\xi_{\text{DM}}(r)}{\sigma_8^2}, \quad (11b)$$

$$\xi_2(s) = \left(\frac{4}{3}\beta + \frac{4}{7}\beta^2\right) [\xi(r) - \bar{\xi}(r)] \quad (12a)$$

$$= \left[\frac{4}{3}f\sigma_8 \cdot b\sigma_8 + \frac{4}{7}(f\sigma_8)^2 \right] \left[\frac{\xi_{\text{DM}}(r)}{\sigma_8^2} - \frac{\bar{\xi}_{\text{DM}}(r)}{\sigma_8^2} \right], \quad (12b)$$

$$\xi_4(s) = \frac{8}{35}\beta^2 \left[\xi(r) + \frac{5}{2}\bar{\xi}(r) - \frac{7}{2}\bar{\xi}(r) \right] \quad (13a)$$

$$= \frac{8}{35}(f\sigma_8)^2 \left[\frac{\xi_{\text{DM}}(r)}{\sigma_8^2} + \frac{5}{2}\frac{\bar{\xi}_{\text{DM}}(r)}{\sigma_8^2} - \frac{7}{2}\frac{\bar{\xi}_{\text{DM}}(r)}{\sigma_8^2} \right], \quad (13b)$$

where $\xi(r)$ and $\xi_{\text{DM}}(r)$ are the real-space *undistorted* correlation functions of tracers and DM, respectively, whereas the *barred* functions are:

$$\bar{\xi}_{\text{DM}}(r) \equiv \frac{3}{r^3} \int_0^r dr' \xi_{\text{DM}}(r') r'^2, \quad (14)$$

$$\bar{\bar{\xi}}_{\text{DM}}(r) \equiv \frac{5}{r^5} \int_0^r dr' \xi_{\text{DM}}(r') r'^4. \quad (15)$$

Eqs. (11b), (12b) and (13b) are derived from Eqs. (11a), (12a) and (13a) respectively, using Eq. (7). In this analysis, $\xi_{\text{DM}}(r)$ is estimated by Fourier transforming the linear power spectrum computed with the software CAMB (Lewis & Bridle 2002) for the cosmological model here considered, while $\xi(r)$ is either measured directly from the real-space mock catalogues, or computed through Eq. (9) assuming a value of the linear bias.

Eq. (10) is an effective description of RSD only at large scales, where non-linear effects are negligible. An empirical model that can account for both linear and non-linear dynamics is the so-called dispersion model (Peacock & Dodds 1996; Peebles 1980; Davis & Peebles 1983), that describes the redshift-space correlation function as a convolution of the linearly-distorted correlation with the distribution function of pairwise velocities, $f(v)$:

$$\xi(s_{\perp}, s_{\parallel}) = \int_{-\infty}^{\infty} dv f(v) \xi \left(s_{\perp}, s_{\parallel} - \frac{v(1+z)}{H(z)} \right)_{\text{lin}}, \quad (16)$$

where the pairwise velocity v is expressed in physical coordinates.

Since we are not considering redshift errors, we use the exponential form for $f(v)$ (Marulli et al. 2012), namely:

$$f(v) = \frac{1}{\sigma_{12}\sqrt{2}} \exp \left(-\frac{\sqrt{2}|v|}{\sigma_{12}} \right) \quad (17)$$

(Davis & Peebles 1983; Fisher, Scharf & Lahav 1994; Zurek et al. 1994). The quantity σ_{12} can be interpreted as the dispersion in the pairwise random peculiar velocities, and is assumed to be independent of pair separations.

The dispersion model given by Eqs. (10)-(17) depends on

three free quantities, $f\sigma_8$, $b\sigma_8$ and σ_{12} (since $\xi_{\text{DM}} \propto \sigma_8^2$), and on the reference background cosmology used both to convert angles and redshifts into distances and to estimate the real-space DM two-point correlation function.

4 METHODOLOGY

To measure the two-point correlation functions of our mock samples we make use of the Landy & Szalay (1993) estimator:

$$\xi(r) = \frac{OO(r) - 2OR(r) + RR(r)}{RR(r)}, \quad (18)$$

where $OO(r)$, $OR(r)$ and $RR(r)$ are the fractions of object-object, object-random and random-random pairs, with spatial separation r , in the range $[r - \delta r/2, r + \delta r/2]$, where δr is the bin size. The random catalogues are constructed to be three times larger than the associated mock samples. We compute the correlation functions up to a maximum scale of $r = 50 h^{-1}$ Mpc, both in the parallel and perpendicular directions. As we have verified with a sub-set of mocks, going to higher scales does not change significantly our results, as the constraints on $f\sigma_8$ are mainly determined by the RSD signal at smaller scales.

To model RSD and extract constraints on $f\sigma_8$, we exploit the model given by Eqs. (10)-(17). We consider two case studies. The first one consists in modelling only the monopole of the redshift-space two-point correlation function at large scales, via Eq. (11b), that is in the Kaiser limit. In this case, non-linear effects are not modelled, as they can be neglected at the scales considered, and the $b\sigma_8$ factor has to be fixed a priori. When analysing real catalogues, this factor can be determined either directly with the deprojection technique (see e.g. Marulli et al. 2012), or from the three-point correlation function (see e.g. Moresco et al. 2014), or by combining clustering and lensing measurements (see e.g. Sereno et al. 2014). To minimise the uncertainties and systematics possibly present in the above methods, we derive $b\sigma_8$ directly from the real-space two-point correlation functions of our mock tracers, through Eq. (9), while the DM correlation is obtained by Fourier transforming the linear CAMB power spectrum, fixing σ_8 at the value of the *Magnetic* simulation.

The second method considered in this work consists in fully exploiting the redshift-space two-dimensional anisotropic correlation function $\xi(s_{\perp}, s_{\parallel})$. An alternative approach would be to use the multipole moments of the correlation function. The advantage is to reduce the number of observables, thus helping in the computation of the covariance matrix (e.g. de la Torre et al. 2013; Petracca et al. in preparation). However, we are not mimicking here any real redshift survey. Thus, a detailed treatment of the statistical errors is not necessary for the purposes of the present paper, that focuses instead on the systematic uncertainties caused by a poor modelization of non-linear effects. Therefore, we will use just diagonal covariance matrices, whose elements are estimated analytically from Poisson statistics. Moreover, to investigate the accuracy of the dispersion model as a function of scales, it is more convenient to exploit $\xi(s_{\perp}, s_{\parallel})$. Indeed, following this approach, we can explore the full $r_{\parallel} - r_{\perp}$ plane, searching for the optimal region to be used to minimise model uncertainties.

5 RESULTS

In this section, we present our main results obtained from mock samples of three different tracers – galaxies, clusters and AGN

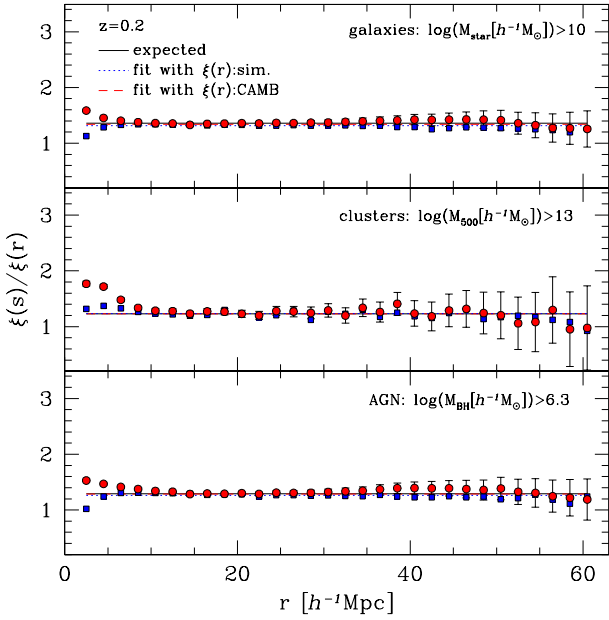


Figure 1. The ratio between the redshift-space and real-space two-point spherically averaged correlation functions, $\xi(s)/\xi(r)$, at $z = 0.2$, for galaxies with $\log(M_{\text{STAR}}[h^{-1}M_{\odot}]) > 10$ (top panel), clusters with $\log(M_{500}[h^{-1}M_{\odot}]) > 13$ (central panel), and AGN with $\log(M_{\text{BH}}[h^{-1}M_{\odot}]) > 6.3$ (bottom panel). The redshift-space correlation functions have been measured directly from the simulation, while the real-space ones have been measured either from the simulation (red dots), or derived from the CAMB power spectrum (blue squares). The error bars represent the statistical noise as prescribed by Mo, Jing & Boerner (1992). The black solid lines show the expected values of $\xi(s)/\xi(r)$ at large scales predicted by Eq. (11b). The dotted blue and dashed red lines are the best-fit ratios estimated from the blue and red points, respectively.

– using the two approaches described in §4. For each catalogue, we analyse six snapshots corresponding to the redshifts $z = \{0.2, 0.52, 0.72, 1, 1.5, 2\}$. Moreover, at each redshift we consider different sample selections. In total, we analyse 270 mock catalogues, whose main properties, including the number of objects in each sample, are reported in Tables A1, A2 and A3, and in Fig. A1 in Appendix A.

5.1 The linear growth rate from the clustering monopole

We start analysing the spherically averaged two-point correlation function – the clustering monopole – at large linear scales. The aim of this exercise is to investigate the accuracy of the dispersion model in the simplest case possible, that is in the so-called Kaiser limit.

Fig. 1 shows the ratio between the redshift-space and real-space two-point correlation functions, $\xi(s)/\xi(r)$. Specifically, we show here the results obtained at $z = 0.2$, for galaxies with $\log(M_{\text{STAR}}[h^{-1}M_{\odot}]) > 10$, clusters with $\log(M_{500}[h^{-1}M_{\odot}]) > 13$, and AGN with $\log(M_{\text{BH}}[h^{-1}M_{\odot}]) > 6.3$, as reported by the labels. These correspond to the upper left samples reported in Tables A1, A2 and A3. Results obtained from the other mock samples are similar, but more scattered due to the lower densities. The redshift-space correlation functions have been measured directly from the simulation, through the procedure described in §4. The real-space correlation functions have been estimated in two different ways.

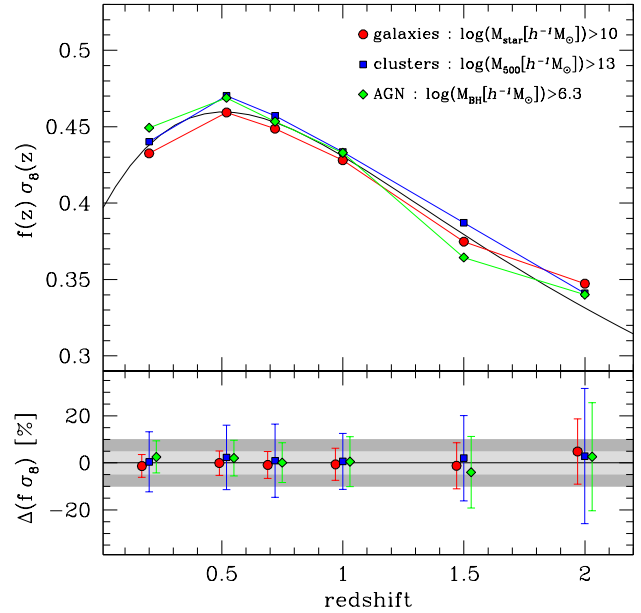


Figure 2. Top panel: the best-fit values of $f(z)\sigma_8(z)$ for galaxies with $\log(M_{\text{STAR}}[h^{-1}M_{\odot}]) > 10$ (red dots), clusters with $\log(M_{500}[h^{-1}M_{\odot}]) > 13$ (blue squares), and AGN with $\log(M_{\text{BH}}[h^{-1}M_{\odot}]) > 6.3$ (green diamonds), obtained with the method described in §5.1. The black line shows the function $\Omega_M(z)^{0.545} \cdot \sigma_8(z)$, where $\Omega_M(z)$ and $\sigma_8(z)$ are the known values of the simulation. Bottom panel: the percentage systematic errors on $f(z)\sigma_8(z)$, $[(f\sigma_8)^{\text{measured}} - (f\sigma_8)^{\text{simulation}}] / (f\sigma_8)^{\text{simulation}} \cdot 100$, that is the percentage differences between the points and the black line shown in the top panel. The error bars have been estimated with Eq. (19). The values reported have been slightly shifted for visual clarity. To guide the eyes, the light and grey shaded areas highlight the 5% and 10% error regions, respectively.

Either they are measured directly from the simulation, or they are derived from the linear CAMB power spectrum, and assuming a linear bias factor. The differences at small scales, $r \lesssim 5 h^{-1} \text{Mpc}$, between the ratios computed with the measured (blue squares) and CAMB (red dots) real-space correlation functions are due to non-linear effects. We verified that using the non-linear CAMB power spectrum, via the HALOFIT routine (Smith et al. 2003), does not fully remove the discrepancy. Nevertheless, as we model here the large scale clustering, this has no effects on our results. On the other hand, the small discrepancies at scales $r \gtrsim 40 h^{-1} \text{Mpc}$ can introduce systematics, that however result smaller than the estimated uncertainties. The error bars in Fig. 1 show the statistical Poisson noise (Mo, Jing & Boerner 1992). Scales larger than $60 h^{-1} \text{Mpc}$, not shown in the plot, are too noisy to affect the fit. More specifically, we verified that a convenient scale range to get robust results is $10 < r[h^{-1} \text{Mpc}] < 50$. The black solid lines show the expected values of $\xi(s)/\xi(r)$ at large scales, as predicted by Eq. (11b).

By modelling the clustering ratio, $\xi(s)/\xi(r)$, via Eq. (11a), it is possible to estimate the factor β . We do this by measuring both $\xi(s)$ and $\xi(r)$ from the simulation. The result is shown by the dotted blue lines in Fig. 1. Instead, to estimate $f\sigma_8$ from the monopole of the two-point correlation function, we use Eq. (11b). In this case the factor $b\sigma_8$ has to be fixed. This requires to estimate the real-space two-point correlation function of the DM. As described above, we obtain the latter by Fourier transforming the CAMB power spectrum. Moreover, to estimate the mean linear bias, a range of scales

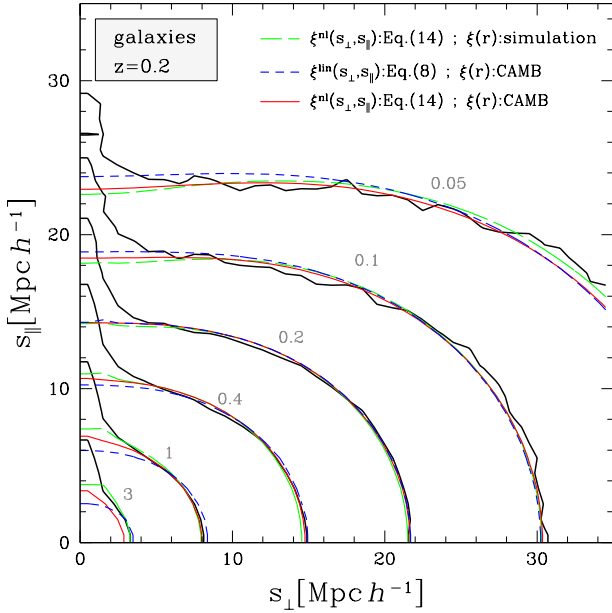


Figure 3. The iso-correlation contours of the redshift-space two-point correlation function, corresponding to the values $\xi(s_{\perp}, s_{\parallel}) = [0.05, 0.1, 0.2, 0.4, 1, 3]$, for galaxies with $\log(M_{\text{STAR}}[h^{-1} M_{\odot}]) > 10$, at $z = 0.2$ (black contours). The dot-dashed green and solid red contours show the best-fit model given by Eq. (16), with the real-space correlation function $\xi(r)$ measured from the simulation, and estimated from the CAMB power spectrum, respectively. The blue dashed contours show the linear best-fit model given by Eq. (10) with the CAMB real-space correlation function.

has to be chosen in Eq. (9). We compute the linear bias in the range $10 + \bar{r} < r[h^{-1} \text{Mpc}] < 50$, where \bar{r} is a free parameter. We find that the best value of \bar{r} to minimise the systematics on $f\sigma_8$ depends non trivially on sample selections. The dashed red lines are the best-fit ratios estimated with this method.

As it can be seen by comparing red and blue lines, the two methods provide concordant results, both of them in agreement with the expectation. Indeed, the real-space correlation function provided by CAMB and assuming a linear bias is in reasonable agreement with the one measured directly from the simulation.

The constraints on $f\sigma_8$ as a function of redshift are shown in the upper panel of Fig. 2. As in Fig. 1, we show the results obtained for galaxies with $\log(M_{\text{STAR}}[h^{-1} M_{\odot}]) > 10$, clusters with $\log(M_{500}[h^{-1} M_{\odot}]) > 13$, and AGN with $\log(M_{\text{BH}}[h^{-1} M_{\odot}]) > 6.3$. The black line shows the function $\Omega_M(z)^{0.545} \cdot \sigma_8(z)$, where $\Omega_M(z)$ and $\sigma_8(z)$ are the values of the *Magneticum* simulation. In the lower panel we show the percentage systematic errors on $f\sigma_8$, defined as $[(f\sigma_8)^{\text{measured}} - (f\sigma_8)^{\text{simulation}}] / (f\sigma_8)^{\text{simulation}} \cdot 100$. The error bars have been estimated using the scaling formula presented in Bianchi et al. (2012), that provides the statistical error on the linear growth rate as a function of bias, b , volume, V , and density, n :

$$\frac{\delta\beta}{\beta} \simeq C b^{0.7} V^{-0.5} \exp\left(\frac{n_0}{b^2 n}\right), \quad (19)$$

where $n_0 = 1.7 \cdot 10^{-4} h^3 \text{Mpc}^{-3}$ and $C = 4.9 \cdot 10^2 h^{-1.5} \text{Mpc}^{1.5}$. In this case, these error bars have to be considered just as lower limits, as they have been estimated considering the full two-dimensional anisotropic correlation function $\xi(s_{\perp}, s_{\parallel})$. Moreover, they have been computed in different scale ranges and with different mock tracers.

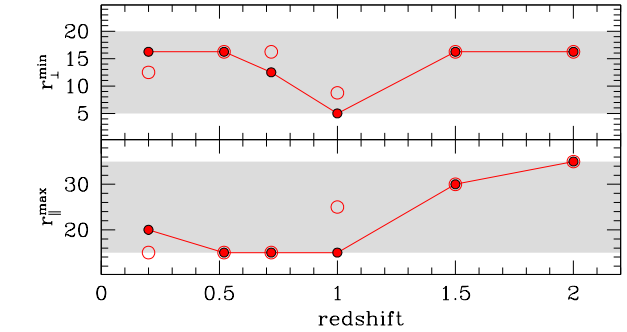
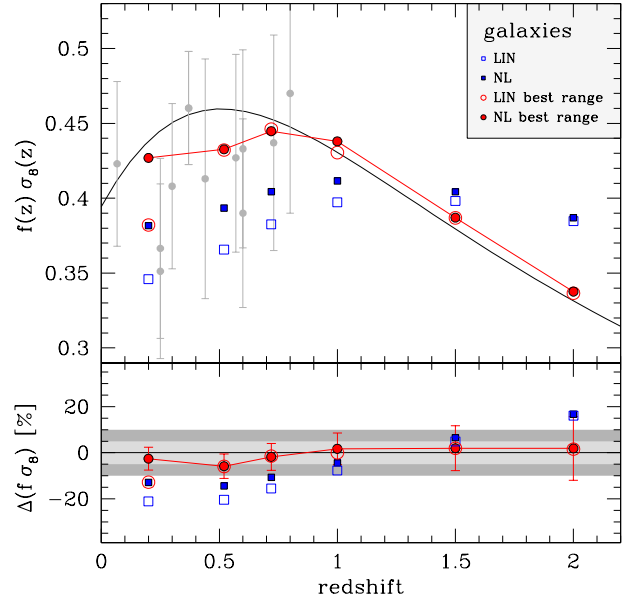


Figure 4. *Top panel of the upper window:* the best-fit values of $f(z)\sigma_8(z)$ for galaxies with $\log(M_{\text{STAR}}[h^{-1} M_{\odot}]) > 10$. The open and solid blue squares show the values obtained by fitting the data with the models given by Eqs. (10) and (16), respectively, in the scale ranges $3 < r_{\perp}[h^{-1} \text{Mpc}] < 35$ and $3 < r_{\parallel}[h^{-1} \text{Mpc}] < 35$. The open and solid red dots have been obtained with the method described in §5.2.1, fitting the data with the models given by Eqs. (10) and (16), respectively. The black line shows the function $\Omega_M(z)^{0.545} \cdot \sigma_8(z)$, where $\Omega_M(z)$ and $\sigma_8(z)$ are the known values of the simulation. For comparison, the grey dots show a set of recent observational measurements from galaxy surveys (see §5.2.1). *Bottom panel of the upper window:* the percentage systematic errors on $f(z)\sigma_8(z)$, defined as $[(f\sigma_8)^{\text{measured}} - (f\sigma_8)^{\text{simulation}}] / (f\sigma_8)^{\text{simulation}} \cdot 100$, that is the percentage differences between the points and the black line shown in the top panel. To guide the eyes, the light and grey shaded areas highlight the 5% and 10% error regions. *Lower window:* best-fit values of r_{\perp}^{min} and $r_{\parallel}^{\text{max}}$ of the method described in §5.2.1. The grey areas show the regions explored by the method.

As demonstrated by Figs. 1 and 2, it is indeed possible to get unbiased constraints on $f\sigma_8$ from the monopole of the two-point correlation function, at all redshifts considered, and for both galaxies, clusters and AGN provided that the linear bias is estimated at sufficiently large scales. The advantage of this method is the minimal number of free parameters necessary for the modelization. However, the linear bias has to be assumed, or measured from other probes.

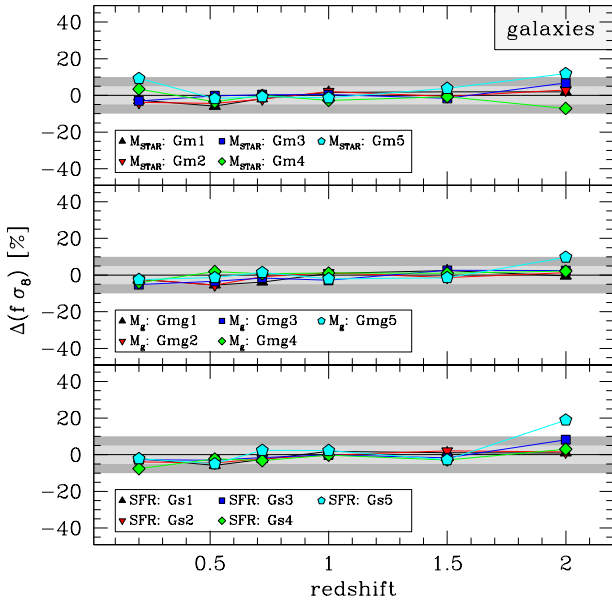


Figure 5. The percentage systematic errors on $f(z)\sigma_8(z)$ for galaxies, $[(f\sigma_8)^{\text{measured}} - (f\sigma_8)^{\text{simulation}}] / (f\sigma_8)^{\text{simulation}} \cdot 100$, as a function of redshift and sample selections, as indicated by the labels. $S1 - S5$ refer to the five selection thresholds reported in Tables A1, A2 and A3, for the different tracers and properties used for the selection.

5.2 The linear growth rate from the anisotropic 2D clustering

To extract the full information from the redshift-space two-point correlation function, the anisotropic correlation $\xi(s_\perp, s_\parallel)$ or, alternatively, all the relevant multipoles have to be modelled. As discussed in §4, we consider the first approach. Differently from the analysis of §5.1, here we can jointly constrain the two terms $f\sigma_8$ and $b\sigma_8$. In this section we investigate the accuracy of the constraints on $f\sigma_8$ provided by the dispersion model, as a function of sample selection, with $b\sigma_8$ and σ_{12} as free parameters.

5.2.1 Galaxies

We start presenting our results for the galaxy mock samples. The black lines of Fig. 3 show the iso-correlation contours of the redshift-space two-point correlation function, $\xi(s_\perp, s_\parallel)$, for galaxies with $\log(M_{\text{STAR}}[h^{-1}M_\odot]) > 10$, at $z = 0.2$. The other lines are the best-fit models obtained with three different methods. The dot-dashed green lines are obtained by using the full non-linear dispersion model given by Eq. (16), with the real-space correlation function $\xi(r)$ measured directly from the simulation. The blue dashed and red solid contours are obtained with $\xi(r)$ estimated from the CAMB power spectrum, and by fitting the linear model given by Eq. (10) and the non-linear one by Eq. (16), respectively. The fitting is done in the scale ranges $3 < r_\perp [h^{-1}\text{Mpc}] < 35$ and $3 < r_\parallel [h^{-1}\text{Mpc}] < 35$.

As one can see, while all the three models provide a good description of the anisotropic clustering at scales larger than $\sim 5 h^{-1}\text{Mpc}$, none of them can reproduce accurately the fingers-of-God pattern at small scales. This is expected for the blue contours, obtained without modelling the non-linear dynamics. For the other two cases, the discrepancy is due to the not sufficiently accurate description of non-linearities provided by the dispersion model. We

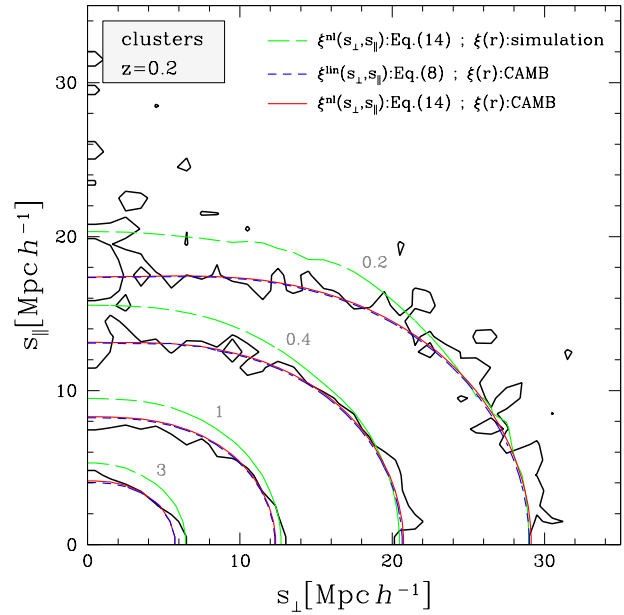


Figure 6. The iso-correlation contours of the redshift-space two-point correlation function, corresponding to the values $\xi(s_\perp, s_\parallel) = [0.2, 0.4, 1, 3]$, for clusters with $\log(M_{500}[h^{-1}M_\odot]) > 13$, at $z = 0.2$ (black contours). The other contours are as in Fig. 3.

verified that the minimum scales considered for the fit have a negligible impact on the fingers-of-God shape. The green contours appear in better agreement with the measurements at small scales, due to the fact that the real-space correlation function is measured from the mock catalogue⁵.

The best-fit values of $f\sigma_8$ as a function of redshift are shown in the top panel of the upper window of Fig. 4. The open and solid blue squares show the values obtained by fitting the data with the models given by Eqs. (10) and (16), respectively, that is they correspond to the blue and red contours of Fig. 3 (at $z = 0.2$). The bottom panel of the upper window shows the percentage systematic errors on $f\sigma_8$, that is $[(f\sigma_8)^{\text{measured}} - (f\sigma_8)^{\text{simulation}}] / (f\sigma_8)^{\text{simulation}} \cdot 100$.

As it can be seen, the best-fit values of $f\sigma_8$ result strongly biased with respect to the true ones, with a systematic error that depends on the redshift. At $z = 0.2$, we get an underestimation of ~ 10 (20) % with the non-linear (linear) dispersion model, at $z = 1$ the error reduces to ~ 5 (8)%, while at $z = 2$ we get an overestimation of $\sim 20\%$, with both linear and non-linear modelling. This result is fairly in agreement with what found by Bianchi et al. (2012) at $z = 1$, although the two analyses are not directly comparable, as Bianchi et al. (2012) considered a sample of Friends-of-Friends DM haloes, slightly affected by fingers-of-God. As expected, the convolution given by Eq. (16) reduces the systematic error on $f\sigma_8$, especially at low redshifts. However, it does not totally remove the discrepancies, in agreement with previous findings. For comparison, the grey dots of Fig. 4 show a set of recent observational measurements of $f\sigma_8$ from large galaxy surveys:

⁵ The model corresponding to the green contours provides constraints on β , not on $f\sigma_8$. We show it here only to highlight the differences at small scales between the dispersion models estimated with $\xi(r)$ measured from the simulation, and the one with $\xi(r)$ from the linear CAMB power spectrum, assuming a linear scale-independent bias.

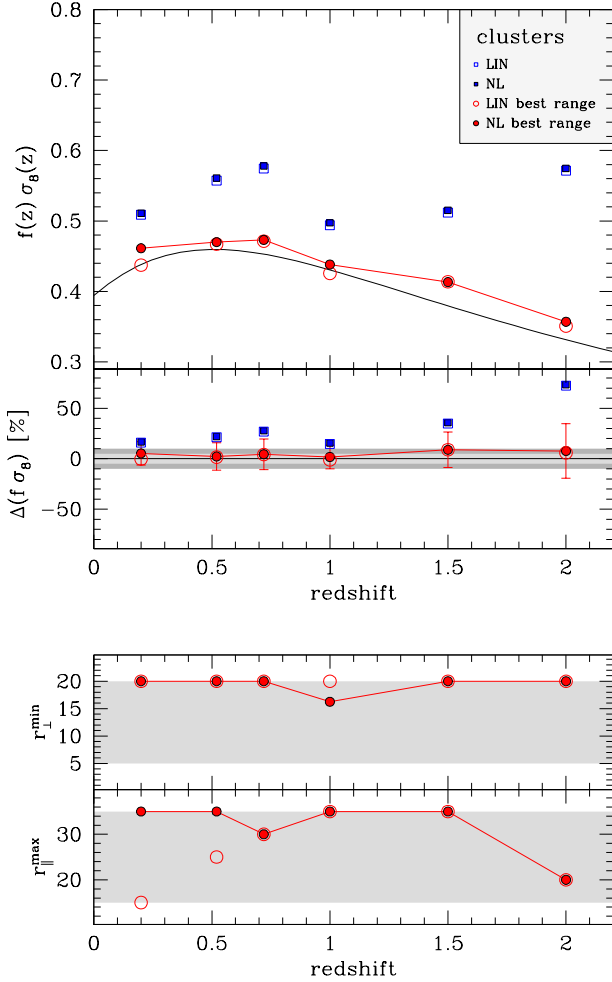


Figure 7. The best-fit values of $f(z)\sigma_8(z)$ for clusters with $\log(M_{500}[h^{-1}M_\odot]) > 13$. All the symbols are as in Fig. 4.

6dFGS at $z = 0.067$ (Beutler et al. 2012); SDSS(DR7) Luminous Red Galaxies at $z = 0.25, 0.37$ (Samushia, Percival & Raccanelli 2012) from scales lower than 60 and 200 h^{-1} Mpc; BOSS at $z = 0.3, 0.57, 0.6$ (Tojeiro et al. 2012; Reid et al. 2012); WiggleZ at $z = 0.44, 0.6, 0.73$ (Blake et al. 2012); VIPERS at $z = 0.8$ (de la Torre et al. 2013). Interestingly, many of these measurements underestimate $f\sigma_8$ with respect to GR predictions (see e.g. Macaulay, Wehus & Eriksen 2013). According to our findings, this might be caused by model uncertainties, rather than by inconsistencies with GR.

The direct way to reduce these systematics is to improve the modelization of RSD at non-linear scales. We explore here a different approach, investigating the dependency of the systematic error on the comoving scales considered in the analysis. Specifically, we repeat our fitting procedure for different values of the parameters r_\perp^{\min} and r_\parallel^{\max} , that is the minimum perpendicular separation and the maximum parallel separation used in the fit. As we verified, changing also r_\perp^{\max} and r_\parallel^{\min} does not affect significantly the results. The aim here is to search for optimal regions in this plane to possibly get unbiased constraints. As non-linear dynamics impact on different scales for different redshifts and biases of the tracers, we expect that the best values of r_\perp^{\min} and r_\parallel^{\max} , that is the

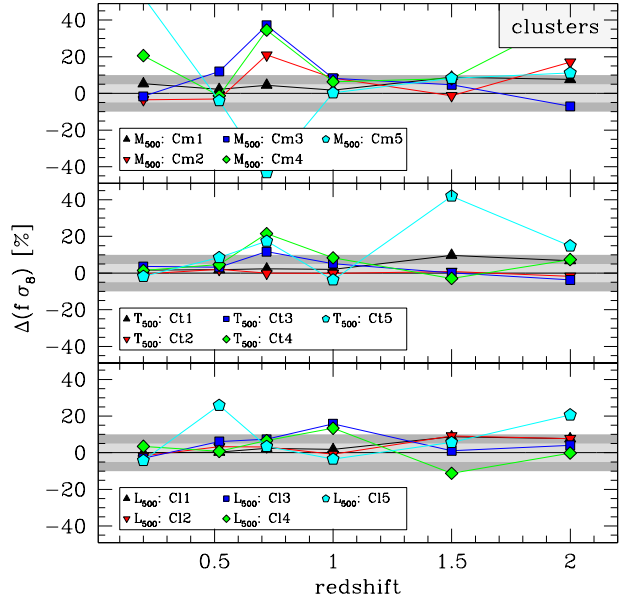


Figure 8. The percentage systematic errors on $f(z)\sigma_8(z)$ for clusters, as a function of redshift and sample selections. All symbols are as in Fig. 5.

ones that minimise systematics, will be different for different sample selections. We explore the ranges $5 < r_\perp^{\min}[h^{-1} \text{Mpc}] < 20$ and $15 < r_\parallel^{\max}[h^{-1} \text{Mpc}] < 35$, highlighted by the grey areas in the bottom panels of the lower window of Fig. 4, that result large enough to get systematic errors on $f\sigma_8$ lower than $\sim 5\%$.

The results of this analysis are shown in Fig. 4 with open and solid red dots, obtained by fitting the data with the model given by Eqs. (10) and (16), respectively. As one can see, for proper values of r_\perp^{\min} and r_\parallel^{\max} , shown in bottom panels of the lower window, it is indeed possible to significantly reduce the systematic error on $f\sigma_8$ at all redshifts, without having to improve the treatment of non-linearities. As shown in the bottom panel of the upper window, the percentage systematic errors on $f\sigma_8$ are lower than 5% at all redshifts. The error bars have been estimated using the scaling formula given by Eq. 19. As in Fig. 2, this should be considered just as an approximate indication of the true errors, as Bianchi et al. (2012) derived the latter by modelling RSD at different scales and with different mock tracers.

Another interesting result shown in Fig. 2 is that both the linear and non-linear dispersion models provide similar results when r_\perp^{\min} and r_\parallel^{\max} are kept free. Indeed, it seems more convenient to simply not consider the scales where non-linear effects have a non-negligible impact, rather than to try modelling them with the empirical description provided by Eq. (16).

We then apply our method to several subsamples with different selections. Specifically, we consider galaxy catalogues selected in stellar mass, M_{STAR} , g-band absolute magnitude, M_g , and star formation rate, SFR. The selection thresholds considered and the number of galaxies in each sample are reported in Table A1. The percentage systematic errors on $f\sigma_8$ are reported in Fig. 5, as a function of redshift and sample selections, as indicated by the labels. The result is quite remarkable: it is indeed possible to get almost unbiased constraints on $f\sigma_8$ with the dispersion model, independent of sample selections, provided that r_\perp^{\min} and r_\parallel^{\max} are chosen conveniently. For the largest galaxy sample shown in Fig. 2, the

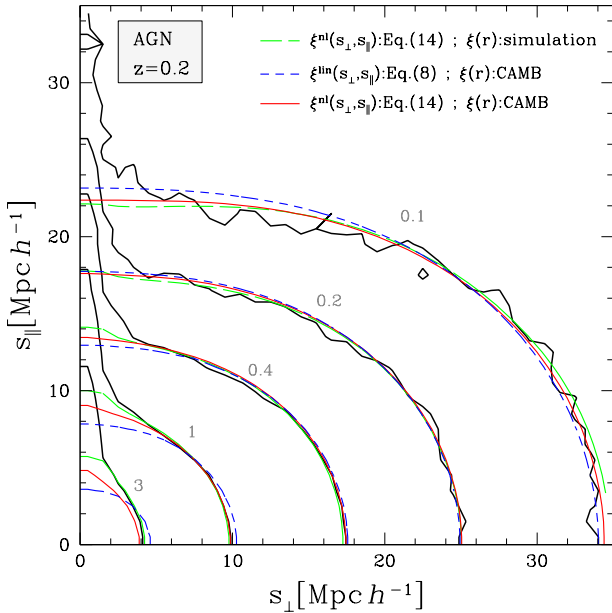


Figure 9. The iso-correlation contours of the redshift-space two-point correlation function, corresponding to the values $\xi(s_{\perp}, s_{\parallel}) = [0.1, 0.2, 0.4, 1, 3]$, for AGN with $\log(M_{\text{BH}}[h^{-1} M_{\odot}]) > 6.3$, at $z = 0.2$ (black contours). The other contours show the best-fit models, as in Fig. 3.

preferred value of r_{\perp}^{min} is $\sim 15 h^{-1} \text{Mpc}$ at low and high redshifts, and $\sim 5 h^{-1} \text{Mpc}$ around $z = 1$, while $r_{\parallel}^{\text{max}}$ is $\sim 15 h^{-1} \text{Mpc}$ at low redshifts, and increases up to $\sim 35 h^{-1} \text{Mpc}$ at $z = 2$. Overall, we did not find however any clear trend of r_{\perp}^{min} and $r_{\parallel}^{\text{max}}$ as a function of redshift or sample bias, possibly due to the not sufficiently large volumes analysed.

5.2.2 Galaxy groups and clusters

In this section, we perform the same analysis presented in §5.2.1 on the mock samples of galaxy groups and clusters. To simplify the discussion, in the following we will use the term *clusters* to refer to all of these objects, though the less massive ones should be considered as galaxy groups, or just haloes, from an observational perspective (see Table A2).

Fig. 6 shows the iso-correlation contours of the redshift-space two-point correlation function of clusters with $\log(M_{500}[h^{-1} M_{\odot}]) > 13$, at $z = 0.2$. The other contours are the best-fit models, as in Fig. 3. As it can be seen, the fingers-of-God anisotropies are almost absent, differently from the galaxy correlation function shown in Fig. 3, due to the lower values of non-linear motions of clusters at small scales. This makes the convolution of Eq. (16) negligible, as it can be seen comparing the dashed blue and solid red lines. Interestingly, when the real-space correlation function $\xi(r)$ is measured from the mocks (green contours), the dispersion model fails to match the small-scale clustering shape. This is primarily caused by the paucity of the cluster sample. Due to the low number of cluster pairs at small separations, the small-scale clustering cannot be estimated accurately, thus introducing systematics in the model. On the contrary, when $\xi(r)$ is estimated from CAMB, the small-scale clustering shape can be accurately described. For visual clarity, we have shown here only

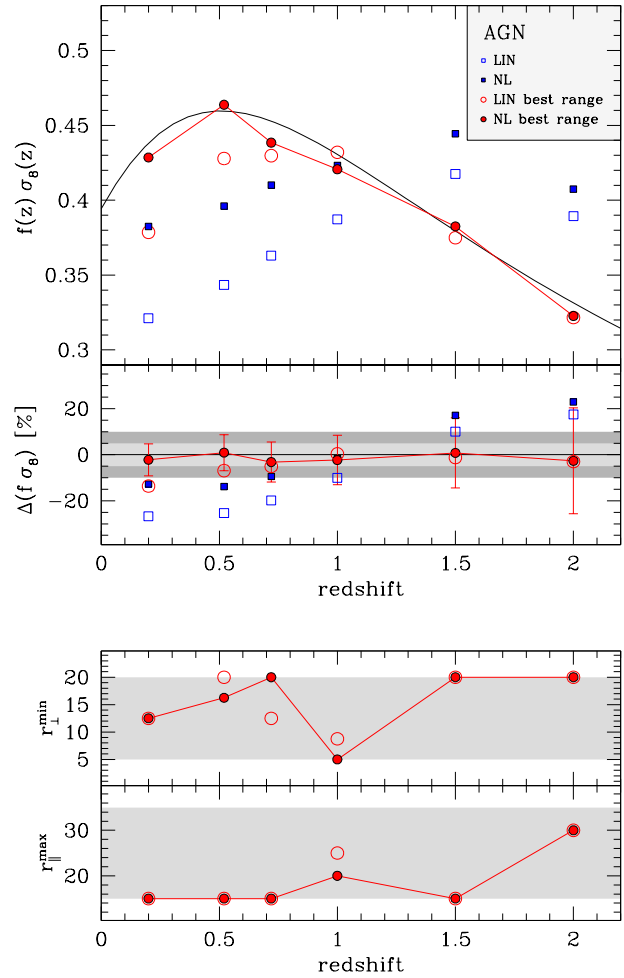


Figure 10. The best-fit values of $f(z)\sigma_8(z)$ for AGN with $\log(M_{\text{BH}}[h^{-1} M_{\odot}]) > 6.3$. All the symbols are as in Fig. 4.

the iso-correlation contours down to $\xi(s_{\perp}, s_{\parallel}) = 0.2$, as for lower values they appear too scattered.

Fig. 7 shows the best-fit values of $f\sigma_8$ as a function of redshift. In contrast to what we found with galaxies, the constraints on the linear growth rate obtained in the scale ranges $3 < r_{\perp}[h^{-1} \text{Mpc}] < 35$ and $3 < r_{\parallel}[h^{-1} \text{Mpc}] < 35$ (blue squares) result severely over-estimated at all redshifts, independent of using the linear or the non-linear dispersion model. To investigate how these systematics depend on the scale range considered in the fit, we repeat the same analysis described in §5.2.1, keeping free the parameters r_{\perp}^{min} and $r_{\parallel}^{\text{max}}$. The result is shown by the red dots in Fig. 7. As one can see, we are able to substantially reduce the systematics on $f\sigma_8$, at all redshifts. This is obtained by cutting the small perpendicular separations, limiting the analysis at $r_{\perp} \gtrsim 20 h^{-1} \text{Mpc}$, as shown in the lower window of Fig. 7.

Then, we consider several cluster subsamples selected in mass, M_{500} , temperature, T_{500} , and luminosity, L_{500} , whose main properties are reported in Table A2⁶. Fig. 8 shows the percentage systematic errors on $f\sigma_8$ as a function of redshift and sample selec-

⁶ M_{500} , T_{500} and L_{500} are, respectively, the mass, the temperature and the luminosity enclosed within a sphere of radius r_{500c} , in which the mean mat-

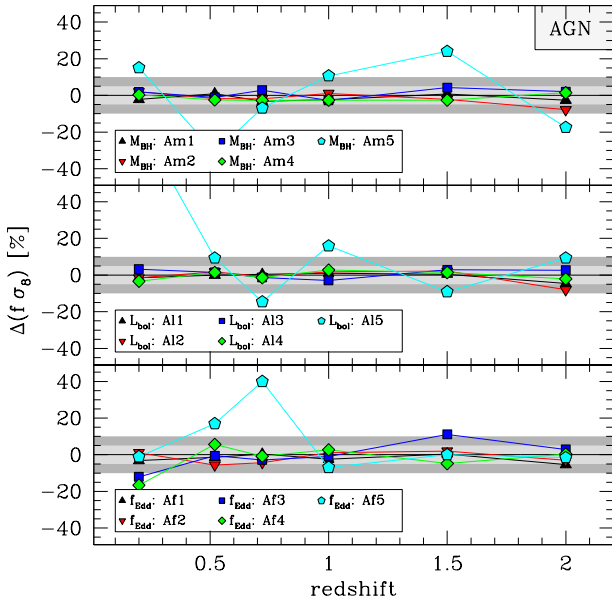


Figure 11. The percentage systematic errors on $f(z)\sigma_8(z)$ for AGN, as a function of redshift and sample selections. All symbols are as in Fig. 5.

tions. For the largest samples analysed we do not get any significant bias on $f\sigma_8$, similarly to what we found with galaxies. However, when selecting too few objects, the results appear quite scattered, though without systematic trends. Indeed, the advantages resulting from the low fingers-of-God anisotropies compensate with the paucity of cluster pairs at small scales. Summarising, it seems possible to get unbiased constraints on the linear growth rate from the RSD of galaxy clusters, but the cluster sample has to be sufficiently numerous.

5.2.3 AGN

Finally, we analyse the AGN mock samples. The results are shown in Figs. 9, 10 and 11, that are the analogous of the plots presented in the previous two sections for galaxies and clusters. As expected, we find similar results to the ones found with galaxies. Differently from the cluster case, the fingers-of-God are clearly evident in the AGN correlation function, and not accurately modelled by the dispersion model, as it can be seen in Fig. 9. Nevertheless, the convolution of Eq. (16) significantly helps in reducing the systematic error on $f\sigma_8$, even more than what we found when analysing the galaxy sample, as evident by comparing Figs. 3 and 9. Also in this case, it is possible to get almost unbiased constraints on $f\sigma_8$ at all redshifts and for the different selections considered, provided that the analysis is restricted at $r_{\perp}^{\min} \gtrsim 15 h^{-1} \text{Mpc}$ and $r_{\parallel}^{\max} \lesssim 15 h^{-1} \text{Mpc}$. Specifically, we considered here AGN catalogues selected in BH mass, M_{BH} , bolometric luminosity, L_{bol} , and Eddington factor, f_{Edd} , as reported in Table A3. Only the AGN samples with the lower number of objects analysed here (cyan points in Fig. 11) are not large enough to provide robust constraints on $f\sigma_8$.

ter density is equal to 500 times the critical density $\rho_{\text{crit}}(z) = 3H^2(z)/8\pi G$, where $H(z)$ is the Hubble parameter.

6 CONCLUSIONS

Clustering anisotropies in redshift-space are one of the most effective probes to test Einstein’s General Relativity on large scales. Though only galaxy samples have been considered so far for these analyses, other astronomical tracers, such as clusters and AGN, will be used in the next future, aimed at maximising the dynamic and redshift ranges where to constrain the linear growth rate of cosmic structures. In particular, clusters of galaxies can be efficiently used to probe the low redshift Universe. Their large bias and low velocity dispersion at small scales make them optimal tracers for large scale structure analyses (Serenio et al. 2014; Veropalumbo et al. 2014, in preparation). On the other hand, AGN samples can be exploited to push the GR test on larger redshifts.

In this work, we made use of both galaxy, cluster and AGN mock samples extracted from the *Magneticum*, a cosmological hydrodynamic simulation of the standard ΛCDM Universe, to investigate the accuracy of the widely used dispersion model as a function of scale and sample selection. Instead of analysing the clustering multipoles, we preferred to extract $f\sigma_8$ constraints from the monopole only, or from the full 2D anisotropic correlation $\xi(s_{\perp}, s_{\parallel})$. This allowed us to explore the $r_{\perp} - r_{\parallel}$ plane, aimed at finding the optimal range of scales to minimise systematic uncertainties.

The main results of this analysis are the following.

- It is possible to get unbiased constraints on $f\sigma_8$ by modelling the large-scale monopole of the two-point correlation function with the Kaiser limit of the dispersion model (Eq. 11b), provided that the linear bias factor $b\sigma_8$ is known. The latter has to be estimated at sufficiently large scales, to avoid non-linearities. With real data, the linear bias can be estimated either with the deprojection technique, or from the three-point correlation function, or by combining clustering and lensing measurements (see the discussion in §4).
- When higher multipoles are considered, $f\sigma_8$ and $b\sigma_8$ can be jointly constrained, and the statistical error on $f\sigma_8$ is substantially reduced (see e.g. Petracca et al. in preparation). However, systematic errors can arise if non-linearities are not treated accurately, such as with the dispersion model (Eqs. 10-17). On the other hand, the analysis shown in this paper demonstrates that it is still possible to get unbiased constraints on $f\sigma_8$ if the range of scales used to model RSD is chosen appropriately. The latter depends on the properties of the tracers.
- If the linear growth rate is estimated from the RSD of either galaxies or AGN, the value of $f\sigma_8$ will be underestimated at $z \lesssim 1$, and overestimated at larger redshifts, when the fit is performed in the fixed range of scales $3 < r_{\perp} [h^{-1} \text{Mpc}] < 35$. With $r_{\perp}^{\min} \sim 15 h^{-1} \text{Mpc}$ and $r_{\parallel}^{\max} \sim 20 h^{-1} \text{Mpc}$, we get almost unbiased constraints. However, the proper values of r_{\perp}^{\min} and r_{\parallel}^{\max} depend on sample selection, and should be fixed differently for each sample analysed, calibrating the analysis using specific mock catalogues.
- If the RSD of galaxy groups and clusters are modelled in the range of scales $3 < r_{\perp} [h^{-1} \text{Mpc}] < 35$, the value of $f\sigma_8$ results severely overestimated at all redshifts. The systematic error can be reduced if the fit is performed at larger scales, as expected due to the low number of cluster pairs at small separations. Specifically, with $r_{\perp}^{\min} \sim 20 h^{-1} \text{Mpc}$ and $r_{\parallel}^{\max} \sim 35 h^{-1} \text{Mpc}$, we get unbiased constraints, but only for the densest group samples. The paucity of the most massive cluster samples does not allow us to obtain robust results.

To summarise, as the dispersion model cannot accurately describe the non-linear motions at small scales, the constraints on

$f\sigma_8$ can be biased. At the present time, it is difficult to include model uncertainties in this kind of analyses, and even more to improve the RSD modelling (see e.g. de la Torre & Guzzo 2012; Bianchi, Chiesa & Guzzo 2015, and references therein). Instead of trying to improve the model, in this analysis we investigated how the systematic errors on the linear growth rate caused by model uncertainties depend on the comoving scales considered. Fortunately, as we have shown, in order to reduce these systematics it is sufficient to restrict the analysis in a proper subregion of the $r_\perp - r_\parallel$ plane. More specifically, we found that it is enough to choose a proper value for r_\perp^{\min} and r_\parallel^{\max} . Indeed, as we verified, changing also r_\perp^{\max} and r_\parallel^{\min} does not affect significantly the results. The drawback of this approach is to inevitably increase the statistic error on $f\sigma_8$. Moreover, the $r_\perp - r_\parallel$ region to be selected strongly depends on the properties of the tracers, and should be determined using suitable mock catalogues. On the other hand, without a sufficiently accurate modelization of non-linear dynamics, this approach is the only one possible to get unbiased constraints.

This can have a strong impact on multiple tracer analyses (e.g. Blake et al. 2013). To avoid different systematic errors on the linear growth rate estimated from the RSD of different tracers, the $r_\perp - r_\parallel$ plane analysed should be different for each sample. And the same when joining together different redshifts, where RSD constraints can be differently biased.

ACKNOWLEDGMENTS

We acknowledge the support from the grants ASI/INAF n.I/023/12/0 ‘Attività relative alla fase B2/C per la missione Euclid’ and MIUR PRIN 2010-2011 ‘The dark Universe and the cosmic evolution of baryons: from current surveys to Euclid’. L.M. acknowledges financial contributions from contracts and PRIN INAF 2012 ‘The Universe in the box: multiscale simulations of cosmic structure’. K.D. acknowledges the support by the DFG Cluster of Excellence ‘Origin and Structure of the Universe’. We are especially grateful for the support by M. Petkova through the Computational Center for Particle and Astrophysics (C²PAP). Computations have been performed at the ‘Leibniz-Rechenzentrum’ with CPU time assigned to the Project ‘pr86re’, as well as at the ‘Rechenzentrum der Max-Planck- Gesellschaft’ at the ‘Max-Planck-Institut für Plasmaphysik’ with CPU time assigned to the ‘Max-Planck-Institut für Astrophysik’. Information on the *Magneticum Pathfinder* project is available at <http://www.magneticum.org>.

APPENDIX A: THE MAIN PROPERTIES OF THE SELECTED SAMPLES

Tables A1, A2 and A3 report the main properties of the mock samples analysed in this work. We consider only integral catalogues. The quantities *min* and *max* reported in the Tables are the minimum and maximum thresholds used for the selections, while *median* is the median of the sample distributions. As it can be seen, we adopt suitable sample selections to have a minimum of ~ 50000 objects in the smallest galaxy samples, and ~ 10000 objects in the smallest cluster and AGN samples. As an illustrative example, Fig. A1 shows the number of mock galaxies, clusters and AGN as a function of redshift, for three different selections, as indicated by the labels.

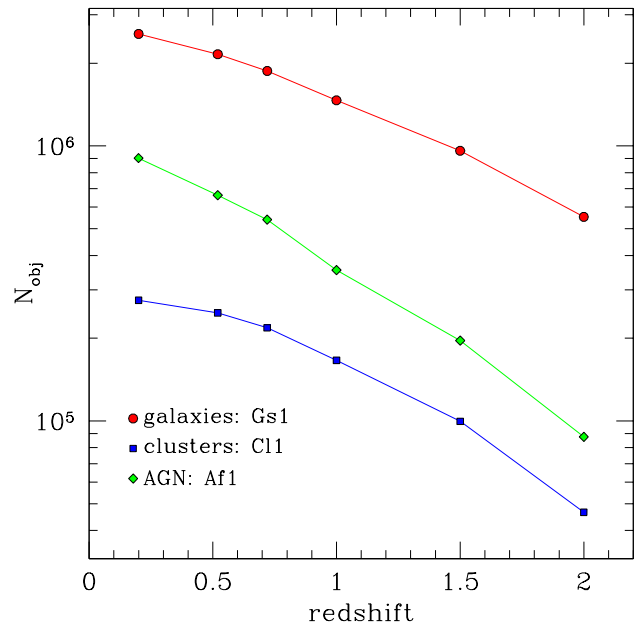


Figure A1. The number of mock galaxies (*red dots*), clusters (*blue squares*) and AGN (*green diamonds*) as a function of redshift, for the three selections: Gs1, C11, Af1 (see Tables A1, A2 and A3).

Table A1. Main properties of the samples of galaxies analysed in the paper.

redshift	$\log(M_{\text{STAR}} [h^{-1} M_{\odot}])$					M_g					$\log(\text{SFR}[M_{\odot}/\text{year}])$				
	sample	min	max	median	objects	sample	min	max	median	objects	sample	min	max	median	objects
0.2	Gm1	10.00	13.24	10.78	2565412	Gmg1	-20.00	-27.39	-21.90	2555977	Gs1	1.00	3.40	1.38	1460374
	Gm2	10.45		10.98	1881270	Gmg2	-20.94		-21.93	2465212	Gs2	1.24		1.47	1057208
	Gm3	10.90		11.13	1080529	Gmg3	-21.87		-22.31	1333968	Gs3	1.48		1.64	509094
	Gm4	11.35		11.55	255117	Gmg4	-22.81		-23.19	267639	Gs4	1.72		1.86	169018
	Gm5	11.79		11.96	50000	Gmg5	-23.74		-24.12	49995	Gs5	1.96		2.08	49996
0.52	Gm1	10.00	13.10	10.73	2167365	Gmg1	-20.00	-27.08	-21.65	2154603	Gs1	1.00	3.33	1.45	1432387
	Gm2	10.42		10.93	1556875	Gmg2	-20.88		-21.70	1985640	Gs2	1.27		1.54	1087917
	Gm3	10.84		11.11	905634	Gmg3	-21.76		-22.21	913480	Gs3	1.54		1.71	550535
	Gm4	11.27		11.46	245678	Gmg4	-22.64		-23.07	231625	Gs4	1.80		1.95	181393
	Gm5	11.69		11.84	50000	Gmg5	-23.52		-23.88	49993	Gs5	2.07		2.20	49998
0.72	Gm1	10.00	13.03	10.69	1894509	Gmg1	-20.00	-26.78	-21.53	1872485	Gs1	1.00	3.35	1.50	1360951
	Gm2	10.40		10.90	1347360	Gmg2	-20.86		-21.62	1657323	Gs2	1.28		1.58	1069332
	Gm3	10.81		11.10	788388	Gmg3	-21.72		-22.19	708654	Gs3	1.56		1.75	569550
	Gm4	11.21		11.39	242502	Gmg4	-22.58		-23.05	209604	Gs4	1.84		2.00	190113
	Gm5	11.61		11.77	50000	Gmg5	-23.44		-23.79	49984	Gs5	2.13		2.25	49999
1	Gm1	10.00	12.92	10.62	1507943	Gmg1	-20.00	-26.78	-21.43	1465209	Gs1	1.00	3.41	1.58	1206017
	Gm2	10.37		10.84	1055108	Gmg2	-20.84		-21.55	1229380	Gs2	1.30		1.65	994050
	Gm3	10.75		11.07	620010	Gmg3	-21.69		-22.15	490496	Gs3	1.60		1.81	572970
	Gm4	11.12		11.28	247210	Gmg4	-22.53		-23.09	171265	Gs4	1.89		2.05	199961
	Gm5	11.49		11.65	49999	Gmg5	-23.38		-23.71	49689	Gs5	2.19		2.32	50000
1.5	Gm1	10.00	12.79	10.55	1028296	Gmg1	-20.00	-26.09	-21.28	959724	Gs1	1.00	3.53	1.67	921472
	Gm2	10.33		10.76	711625	Gmg2	-20.79		-21.44	760311	Gs2	1.31		1.72	811432
	Gm3	10.67		10.99	421555	Gmg3	-21.58		-21.96	298389	Gs3	1.62		1.87	516807
	Gm4	11.00		11.19	204649	Gmg4	-22.38		-23.28	86610	Gs4	1.93		2.09	206667
	Gm5	11.33		11.48	50000	Gmg5	-23.17		-23.56	49994	Gs5	2.24		2.37	50000
2	Gm1	10.00	12.49	10.48	618406	Gmg1	-20.00	-25.87	-21.17	552844	Gs1	1.00	3.54	1.74	589434
	Gm2	10.29		10.67	425026	Gmg2	-20.51		-21.27	477671	Gs2	1.31		1.78	543876
	Gm3	10.58		10.88	254679	Gmg3	-21.02		-21.48	330108	Gs3	1.61		1.90	386208
	Gm4	10.87		11.10	130253	Gmg4	-21.53		-21.85	148563	Gs4	1.92		2.11	179827
	Gm5	11.16		11.30	49999	Gmg5	-22.05		-22.49	47889	Gs5	2.23		2.36	49996

Table A2. Main properties of the samples of galaxy groups and clusters analysed in the paper.

redshift	$\log(M_{500}[h^{-1} M_{\odot}])$					$T_{500}[keV]$					$\log(L_{500}[erg/s])$				
	sample	min	max	median	objects	sample	min	max	median	objects	sample	min	max	median	objects
0.2	Cm1	13.00	14.97	13.26	103201	Ct1	0.10	8.27	0.29	274787	Cl1	42.00	46.57	42.51	249655
	Cm2	13.18		13.41	63705	Ct2	0.19		0.35	215729	Cl2	42.41		42.75	153119
	Cm3	13.37		13.58	36858	Ct3	0.34		0.54	110534	Cl3	42.83		43.16	65040
	Cm4	13.55		13.74	19963	Ct4	0.64		0.89	39922	Cl4	43.24		43.54	26922
	Cm5	13.74		13.90	9999	Ct5	1.18		1.52	9902	Cl5	43.66		43.92	9977
0.52	Cm1	13.00	14.97	13.23	84523	Ct1	0.10	7.94	0.30	247341	Cl1	42.00	46.09	42.64	239836
	Cm2	13.16		13.37	53798	Ct2	0.18		0.36	198050	Cl2	42.43		42.78	180659
	Cm3	13.31		13.50	32449	Ct3	0.33		0.52	109150	Cl3	42.87		43.19	75378
	Cm4	13.47		13.64	18518	Ct4	0.61		0.84	40267	Cl4	43.30		43.59	29210
	Cm5	13.62		13.79	10000	Ct5	1.11		1.42	9959	Cl5	43.73		43.98	9991
0.72	Cm1	13.00	14.69	13.22	69404	Ct1	0.10	6.57	0.31	218241	Cl1	42.00	46.24	42.77	215861
	Cm2	13.13		13.33	45804	Ct2	0.18		0.36	176278	Cl2	42.44		42.83	187288
	Cm3	13.27		13.45	29018	Ct3	0.32		0.50	103154	Cl3	42.89		43.20	84083
	Cm4	13.40		13.57	17408	Ct4	0.58		0.80	39329	Cl4	43.33		43.61	31049
	Cm5	13.54		13.69	9999	Ct5	1.04		1.31	9973	Cl5	43.77		44.02	9992
1	Cm1	12.50	14.58	12.81	167773	Ct1	0.10	5.85	0.31	166270	Cl1	42.00	46.15	42.88	166445
	Cm2	12.72		12.97	104160	Ct2	0.17		0.36	137909	Cl2	42.44		42.91	156759
	Cm3	12.95		13.15	55569	Ct3	0.30		0.47	86893	Cl3	42.88		43.20	84056
	Cm4	13.17		13.34	25461	Ct4	0.52		0.72	36186	Cl4	43.32		43.59	32064
	Cm5	13.39		13.54	10000	Ct5	0.91		1.15	9991	Cl5	43.76		43.99	9992
1.5	Cm1	12.50	14.43	12.77	100290	Ct1	0.10	4.83	0.31	99747	Cl1	42.00	46.20	43.06	100220
	Cm2	12.67		12.90	66549	Ct2	0.16		0.35	86504	Cl2	42.44		43.06	98730
	Cm3	12.85		13.04	39631	Ct3	0.27		0.45	57585	Cl3	42.87		43.23	70071
	Cm4	13.02		13.18	21126	Ct4	0.44		0.61	30005	Cl4	43.31		43.60	29699
	Cm5	13.20		13.34	10000	Ct5	0.72		0.92	9975	Cl5	43.75		43.97	9971
2	Cm1	12.50	14.23	12.74	46857	Ct1	0.10	4.17	0.28	46602	Cl1	42.00	45.79	43.21	46857
	Cm2	12.61		12.82	34568	Ct2	0.15		0.31	42502	Cl2	42.40		43.21	46818
	Cm3	12.73		12.91	24316	Ct3	0.22		0.39	30646	Cl3	42.80		43.23	44871
	Cm4	12.84		13.00	15934	Ct4	0.34		0.52	18884	Cl4	43.20		43.52	23962
	Cm5	12.95		13.10	10000	Ct5	0.50		0.68	9934	Cl5	43.60		43.87	9953

Table A3. Main properties of the samples of AGN analysed in the paper.

redshift	$\log(M_{\text{BH}}[h^{-1} M_{\odot}])$					$\log(L_{\text{bol}}[\text{erg/s}])$					$\log(f_{\text{Edd}})$				
	sample	min	max	median	objects	sample	min	max	median	objects	sample	min	max	median	objects
0.2	Am1	6.30	11.05	8.50	946365	A11	40.00	48.21	43.26	903502	Af1	-5.00	0.19	-3.28	900571
	Am2	7.16		8.76	559616	A12	41.49		43.35	820496	Af2	-3.78		-2.82	669586
	Am3	8.02		8.78	530118	A13	42.99		43.67	561712	Af3	-2.57		-1.65	282446
	Am4	8.88		9.13	200602	A14	44.48		45.26	104962	Af4	-1.35		-0.92	100757
	Am5	9.74		9.88	9999	A15	45.97		46.29	9999	Af5	-0.13		0.11	9999
0.52	Am1	6.30	11.03	8.49	687068	A11	40.00	48.27	43.55	662433	Af1	-5.00	0.20	-2.98	664774
	Am2	7.15		8.84	387939	A12	41.55		43.65	602637	Af2	-3.74		-2.75	559834
	Am3	8.00		8.86	368515	A13	43.10		43.93	435109	Af3	-2.47		-1.57	227878
	Am4	8.85		9.12	189324	A14	44.64		45.39	86203	Af4	-1.21		-0.69	74218
	Am5	9.70		9.83	10000	A15	46.19		46.51	9999	Af5	0.05		0.18	9999
0.72	Am1	6.30	10.98	8.18	556411	A11	40.00	48.37	43.65	539859	Af1	-5.00	0.20	-2.80	542532
	Am2	7.14		8.89	298180	A12	41.54		43.76	493217	Af2	-3.75		-2.64	483058
	Am3	7.99		8.92	282007	A13	43.09		44.07	351857	Af3	-2.50		-1.63	216373
	Am4	8.83		9.13	170321	A14	44.63		45.37	85212	Af4	-1.25		-0.70	69112
	Am5	9.67		9.80	9999	A15	46.18		46.44	9999	Af5	0.00		0.16	10000
1	Am1	6.30	10.92	7.99	362513	A11	40.00	48.40	43.91	353674	Af1	-5.00	0.19	-2.63	355647
	Am2	7.13		9.02	194441	A12	41.60		44.03	323269	Af2	-3.72		-2.50	324605
	Am3	7.97		9.05	181542	A13	43.20		44.36	235508	Af3	-2.43		-1.46	154064
	Am4	8.80		9.17	138296	A14	44.80		45.56	69691	Af4	-1.15		-0.46	56167
	Am5	9.63		9.75	9999	A15	46.39		46.65	10000	Af5	0.14		0.18	9959
1.5	Am1	6.30	10.75	7.01	199546	A11	40.00	48.52	44.17	196211	Af1	-5.00	0.20	-2.05	197164
	Am2	7.12		9.14	97867	A12	41.68		44.30	181622	Af2	-3.71		-1.90	186168
	Am3	7.94		9.19	89539	A13	43.36		44.70	133756	Af3	-2.41		-1.05	114389
	Am4	8.75		9.27	73532	A14	45.04		46.14	49508	Af4	-1.12		-0.29	60067
	Am5	9.57		9.69	9999	A15	46.72		46.95	10000	Af5	0.17		0.18	8465
2	Am1	6.30	10.64	6.68	88522	A11	40.00	48.63	44.09	87627	Af1	-5.00	0.20	-1.55	87913
	Am2	7.08		9.13	38422	A12	41.66		44.27	82555	Af2	-3.76		-1.50	85568
	Am3	7.86		9.22	33150	A13	43.31		45.13	56194	Af3	-2.53		-1.13	67129
	Am4	8.64		9.32	27031	A14	44.97		46.31	30473	Af4	-1.30		-0.40	37606
	Am5	9.41		9.57	10001	A15	46.63		46.92	10000	Af5	-0.06		0.18	9988

REFERENCES

- Amendola L., et al., 2013, *Living Reviews in Relativity*, 16, 6
- Beutler F., et al., 2012, *Mon. Not. R. Astron. Soc.*, 423, 3430
- Bianchi D., Chiesa M., Guzzo L., 2015, *Mon. Not. R. Astron. Soc.*, 446, 75
- Bianchi D., Guzzo L., Branchini E., Majerotto E., de la Torre S., Marulli F., Moscardini L., Angulo R. E., 2012, ArXiv e-prints
- Blake C., et al., 2012, *Mon. Not. R. Astron. Soc.*, 425, 405
- Blake C., et al., 2013, *Mon. Not. R. Astron. Soc.*, 436, 3089
- Bocquet S., Saro A., Dolag K., Mohr J. J., 2015, ArXiv e-prints
- Bondi H., 1952, *Mon. Not. R. Astron. Soc.*, 112, 195
- Bondi H., Hoyle F., 1944, *Mon. Not. R. Astron. Soc.*, 104, 273
- Bonoli S., Marulli F., Springel V., White S. D. M., Branchini E., Moscardini L., 2009, *Mon. Not. R. Astron. Soc.*, 396, 423
- Chabrier G., 2003, *Publ. Astron. Soc. Pac.*, 115, 763
- Chuang C.-H. et al., 2013, *Mon. Not. R. Astron. Soc.*, 433, 3559
- Chuang C.-H., Wang Y., 2013, *Mon. Not. R. Astron. Soc.*, 435, 255
- Contreras C., et al., 2013, *Mon. Not. R. Astron. Soc.*, 430, 924
- Davis M., Peebles P. J. E., 1983, *Astrophys. J.*, 267, 465
- de la Torre S., Guzzo L., 2012, ArXiv e-prints
- de la Torre S., et al., 2013, *Astron. Astrophys.*, 557, A54
- Di Matteo T., Springel V., Hernquist L., 2005, *Nature*, 433, 604
- Dolag A., et al., in preparation
- Dolag K., Vazza F., Brunetti G., Tormen G., 2005, *Mon. Not. R. Astron. Soc.*, 364, 753
- Fabjan D., Borgani S., Tornatore L., Saro A., Murante G., Dolag K., 2010, *Mon. Not. R. Astron. Soc.*, 401, 1670
- Ferland G. J., Korista K. T., Verner D. A., Ferguson J. W., Kingdon J. B., Verner E. M., 1998, *Publ. Astron. Soc. Pac.*, 110, 761
- Fisher K. B., Scharf C. A., Lahav O., 1994, *Mon. Not. R. Astron. Soc.*, 266, 219
- Guzzo L., et al., 2008, *Nature*, 451, 541
- Haardt F., Madau P., 2001, in *Clusters of Galaxies and the High Redshift Universe Observed in X-rays*, Neumann D. M., Tran J. T. V., eds., p. 64
- Hamilton A. J. S., 1992, *Astrophys. J. Lett.*, 385, L5
- Hirschmann M., Dolag K., Saro A., Bachmann L., Borgani S., Burkert A., 2014, *Mon. Not. R. Astron. Soc.*, 442, 2304
- Hoyle F., Lyttleton R. A., 1939, *Proceedings of the Cambridge Philosophical Society*, 35, 405
- Kaiser N., 1987, *Mon. Not. R. Astron. Soc.*, 227, 1
- Komatsu E., et al., 2011, *Astrophys. J. Suppl.*, 192, 18
- Landy S. D., Szalay A. S., 1993, *Astrophys. J.*, 412, 64
- Laureijs R., et al., 2011, ArXiv e-prints
- Lewis A., Bridle S., 2002, *Phys. Rev. D*, 66, 103511
- Lilje P. B., Efstathiou G., 1989, *Mon. Not. R. Astron. Soc.*, 236, 851
- Macaulay E., Wehus I. K., Eriksen H. K., 2013, *Physical Review Letters*, 111, 161301
- Marulli F., Baldi M., Moscardini L., 2012, *Mon. Not. R. Astron. Soc.*, 420, 2377
- Marulli F., Bianchi D., Branchini E., Guzzo L., Moscardini L., Angulo R. E., 2012, *Mon. Not. R. Astron. Soc.*, 426, 2566
- Marulli F., Bonoli S., Branchini E., Gilli R., Moscardini L., Springel V., 2009, *Mon. Not. R. Astron. Soc.*, 396, 1404
- Marulli F., Bonoli S., Branchini E., Moscardini L., Springel V., 2008, *Mon. Not. R. Astron. Soc.*, 385, 1846
- Marulli F., Carbone C., Viel M., Moscardini L., Cimatti A., 2011, *Mon. Not. R. Astron. Soc.*, 418, 346
- McGill C., 1990, *Mon. Not. R. Astron. Soc.*, 242, 428
- Merloni A., et al., 2012, ArXiv e-prints
- Mo H. J., Jing Y. P., Boerner G., 1992, *Astrophys. J.*, 392, 452
- Moresco M., Marulli F., Baldi M., Moscardini L., Cimatti A., 2014, *Mon. Not. R. Astron. Soc.*, 443, 2874
- Padovani P., Matteucci F., 1993, *Astrophys. J.*, 416, 26
- Peacock J. A., Dodds S. J., 1996, *Mon. Not. R. Astron. Soc.*, 280, L19
- Peebles P. J. E., 1980, *The large-scale structure of the universe*
- Perlmutter S., et al., 1999, *Astrophys. J.*, 517, 565
- Petracca A., et al., in preparation
- Reid B. A., et al., 2012, *Mon. Not. R. Astron. Soc.*, 426, 2719
- Riess A. G., et al., 1998, *Astron. J.*, 116, 1009
- Samushia L., Percival W. J., Raccanelli A., 2012, *Mon. Not. R. Astron. Soc.*, 420, 2102
- Sargent W. L. W., Turner E. L., 1977, *Astrophys. J. Lett.*, 212, L3
- Saro A., et al., 2014, *Mon. Not. R. Astron. Soc.*, 440, 2610
- Sereno M., Veropalumbo A., Marulli F., Covone G., Moscardini L., Cimatti A., 2014, ArXiv e-prints
- Shakura N. I., Sunyaev R. A., 1973, *Astron. Astrophys.*, 24, 337
- Smith R. E. et al., 2003, *Mon. Not. R. Astron. Soc.*, 341, 1311
- Spergel D., et al., 2013, ArXiv e-prints
- Springel V., 2005, *Mon. Not. R. Astron. Soc.*, 364, 1105
- Springel V., Hernquist L., 2002, *Mon. Not. R. Astron. Soc.*, 333, 649
- Springel V., Hernquist L., 2003a, *Mon. Not. R. Astron. Soc.*, 339, 289
- Springel V., Hernquist L., 2003b, *Mon. Not. R. Astron. Soc.*, 339, 312
- Springel V., et al., 2005, *Nature*, 435, 629
- Thielemann F.-K. et al., 2003, *Nuclear Physics A*, 718, 139
- Tojeiro R., et al., 2012, *Mon. Not. R. Astron. Soc.*, 424, 2339
- Tornatore L., Borgani S., Dolag K., Matteucci F., 2007, *Mon. Not. R. Astron. Soc.*, 382, 1050
- van den Hoek L. B., Groenewegen M. A. T., 1997, *Astron. Astrophys. Suppl.*, 123, 305
- Veropalumbo A., Marulli F., Moscardini L., Moresco M., Cimatti A., 2014, *Mon. Not. R. Astron. Soc.*, 442, 3275
- Veropalumbo A., et al., in preparation
- Wiersma R. P. C., Schaye J., Smith B. D., 2009, *Mon. Not. R. Astron. Soc.*, 393, 99
- Woosley S. E., Weaver T. A., 1995, *Astrophys. J. Suppl.*, 101, 181
- Zurek W. H., Quinn P. J., Salmon J. K., Warren M. S., 1994, *Astrophys. J.*, 431, 559
- Zwicky F., 1937, *Astrophys. J.*, 86, 217